Wavelength Sensitivity of Single Nanowire Excitation Polarization Anisotropies Explained through a Generalized Treatment of Their Linear Absorption

Jay Giblin,[†] Vladimir Protasenko,[‡] and Masaru Kuno[†,*]

[†]University of Notre Dame, Department of Chemistry and Biochemistry, 251 Nieuwland Science Hall, Notre Dame, Indiana 46556 and [‡]University of Notre Dame, Department of Electrical Engineering, 275 Fitzpatrick Hall, Notre Dame, Indiana 46556

ABSTRACT We investigate the excitation polarization anisotropy of individual semiconductor nanowires (NWs) by monitoring their band edge emission above 680 nm in order to clarify the origin of their strong polarization response. Samples studied include both CdSe and CdSe/CdS core/shell nanowires grown using solution chemistry as well as analogous wires made *via* chemical-vapor-deposition (CVD). In the limit of optically thick wires, with radii above ~25 nm, we find NW optical responses consistent with the interaction between strong dielectric contrast influences and the onset of bulk-like behavior. Namely, a sizable wavelength dependence of the excitation polarization anisotropy (ρ_{exc}) exists when NW diameters become comparable to the wavelength of light inside the wire. As a consequence, pronounced ρ_{exc} rolloffs occur at short wavelengths. By contrast, thinner wires do not exhibit such wavelength dependencies, in agreement with earlier studies. We quantitatively explain observed wavelength sensitivities by modeling the NW as an absorbing dielectric cylinder under plane wave excitation. A comparison of predicted ρ_{exc}-values to experimental numbers shows good agreement and confirms the existence of wavelength-dependent ρ_{exc}-values in optically thick wires. Additional results of the model include generalized expressions for NW linear absorption cross-sections under parallel, perpendicular, and circularly polarized excitation. This study therefore adds to a growing body of knowledge about NW polarization anisotropies, specifically, their response in a size regime where dielectric contrast effects compete with the onset of bulk-like behavior.

KEYWORDS: nanowire · CdSe · anisotropy · absorption cross-section · dielectric contrast · core/shell

Unlike most bulk materials, nanowires (NWs) exhibit strong polarization sensitivities in their linear absorption and emission. To date, the existence of prominent NW polarization anisotropies has been explained by invoking one of two mechanisms. The first stems from a sizable dielectric mismatch between NWs and their local surrounding environment.[1] The second originates from confinement-induced valence band mixing.[2,3] In the first case, the magnitude of an electromagnetic wave's electric field inside a NW depends on the orientation of its polarization vector relative to the NW growth axis. Specifically, the parallel and perpendicular components of the electric field ($E_\parallel$, $E_\perp$) are found to be $E_\parallel = E_{0\parallel}$ and $E_\perp = (2\varepsilon_M/(\varepsilon(\omega) + \varepsilon_M))E_{0\perp}$ where $\varepsilon(\omega)$ [(ε_M)] is the dielectric constant of the wire (surrounding medium) and $E_{0\parallel}$ ($E_{0\perp}$) is the parallel (perpendicular) component of the incident light's electric field ($\mathbf{E_0}$).[4] In the second mechanism, size quantization leads to valence band mixing, which strongly alters the underlying polarization sensitivity and selectivity of interband optical transitions.[2,3] This results in an intrinsic source of NW excitation/emission polarization anisotropies.

Evidence for either mechanism exists. Specifically, recent polarization anisotropy measurements on freestanding InP NWs, synthesized *via* laser-assisted catalytic growth, show large excitation/emission polarization anisotropies of ρ_{exc} and $\rho_{emm} \approx$ 0.91 [$\rho_{exc/emm} = (I_\parallel - I_\perp)/(I_\parallel + I_\perp)$, where $I_\parallel$ and $I_\perp$ are the observed photoluminescence intensities with polarization parallel and perpendicular to the NW growth axis].[1] These values have readily been explained by considering the former dielectric contrast mechanism without the need to invoke quantization effects,[5,6] despite NW radii within the confinement regime of InP ($a_B \approx$ 12 nm). Similarly large anisotropies have been observed in other NWs with radii outside their respective confinement regimes.[7−10]

At the same time, prior literature exists on excitation/emission anisotropies from lithographically defined quantum wires.[11−14] Anisotropies of $\rho_{exc} \approx$ 0.4 have

been seen in InGaAs quantum well wires where confinement-induced valence band mixing occurs.[11] In this case, dielectric contrast contributions to the anisotropy could largely be ignored since observed wires were grown/embedded in a medium having a similar dielectric constant. Analogous behavior was also seen in GaAs/AlAs wires where similar ρ_{exc} values were measured.[13] These results, along with corresponding theory,[2,3,15−18] simultaneously support an important role played by confinement in inducing NW polarization anisotropies.

Two sources for sizable NW excitation/emission polarization anisotropies therefore exist. However, ambiguity remains as to the relative contributions from each. Thus clarifying this issue is important since sizable dielectric contrast effects could offer intriguing possibilities for basic and applied NW studies. Specifically, due to the existence of strong dielectric contrast effects, the optical and electrical response of NWs could be varied by simply altering the dielectric constant of the surrounding medium.[19] Not only would polarization anisotropies vary, but so too would exciton binding energies as well as NW linear absorption and emission frequencies. Such effects would then open up new areas of study and would also aid their application in devices. To illustrate, within the context of this study, NWs could be used in polarization sensitive devices such as single wire[1,20] or ensemble[21,22] polarization sensitive photodetectors.

Recently we have prepared narrow diameter CdSe NWs using solution−liquid−solid (SLS) growth[23] and have shown that they exhibit large excitation/emission polarization anisotropies (ρ_{exc} = 0.91, ρ_{emm} = 0.78).[24] As with InP wires, large anisotropies arise from either quantization effects or from dielectric contrast influences, especially since NW radii are nominally within the confinement regime of CdSe (a_B = 5.6 nm). Therefore, to address the origin of these observed anisotropies we have previously investigated whether their magnitude is dictated primarily by confinement or by dielectric contrast through size-, excitation wavelength-, and environment-dependent ρ_{exc} measurements of individual NWs.[24]

Results from these studies suggest that even though confinement may play a role in determining the magnitude of observed ρ_{exc}-values, dielectric contrast influences appear to dominate the overall NW response. Specifically, our study shows no apparent ρ_{exc} wavelength dependencies that one might expect from thin ($r \approx 3$ nm) NWs exhibiting (apparent) confinement effects in their linear absorption. Furthermore, we have demonstrated that embedding NWs in polymethylmethacrylate (PMMA, ε_M = 2.2) substantially decreases measured ρ_{exc}-values ($\Delta\rho_{exc} \approx 0.17$) compared to numbers seen in identical wires at the air/glass interface.[24] As a consequence, these observations suggest that dielectric contrast strongly influences NW anisotropies

and, in turn, reveal prospects for tuning their polarization sensitivity by simply varying the local dielectric environment of the wire.

But having investigated the interplay between dielectric contrast and confinement and having seen that the former dominates, where do dielectric contrast influences end yielding the onset of bulk-like behavior? At some point, with increasing diameter, wires must begin to exhibit bulk-like properties, leading to corresponding drops of their polarization anisotropy. We therefore address this question by exploring the limiting case of optically *thick* NWs where radii begin to have dimensions comparable to the wavelength of light inside the wire ($\lambda_{eff} = \lambda/n_{NW}$ where λ is the incident free space wavelength and n_{NW} is the NW's refractive index).

In this respect, significant ρ_{emm} radial dependencies have recently been observed in GaN nanorods where ρ_{emm}-values decreased when nanorod radii increased above ~25 nm.[25] This was attributed to emission depolarization at large radii due to decreases in dielectric contrast. Additionally, Z. Fan *et al.* have qualitatively observed spectral polarization sensitivities in single ZnO NW transistors while measuring their photoconductivity.[26] However, quantitative ρ_{exc} measurements have not been carried out in either case. As a consequence, this study reports experimental, radial, ρ_{exc} wavelength sensitivities for individual CdSe and core/shell CdSe/CdS NWs with radii between 12 and 36 nm. In tandem, complementary theoretical modeling has been carried out, based on a Poynting vector field analysis where we solve for the transmitted electric and magnetic fields inside a NW under parallel and perpendicularly polarized excitation. Subsequent calculation of the Poynting vector field and its divergence enables us to estimate the absorbed light intensity for these various polarizations. ρ_{exc}-values have then been calculated as a function of wavelength to test for any wavelength dependencies and have yielded excellent agreement with experimental results. A separate outcome of this model has been the derivation of rigorous (generic) expressions for the NW absorption cross-section, which should prove useful for calculating the efficiency of NW light absorption in the absence of actual experimental values.

RESULTS AND DISCUSSION

To study the polarization anisotropy of NWs in a regime where dielectric contrast influences compete with the onset of bulk-like behavior, three types of NWs were prepared. First, SLS growth[23,27−32] was used to prepare CdSe NWs with an average radius of 11.7 ± 4.20 nm. Because current SLS syntheses yield maximum radii on the order of ~15 nm, a portion of these "bare" wires was overcoated with CdS using a procedure described in ref 33. Resulting core/shell CdSe/CdS NWs had a radius of 36.2 ± 12.1 nm. Furthermore, a chemical-vapor-deposition (CVD) approach was used
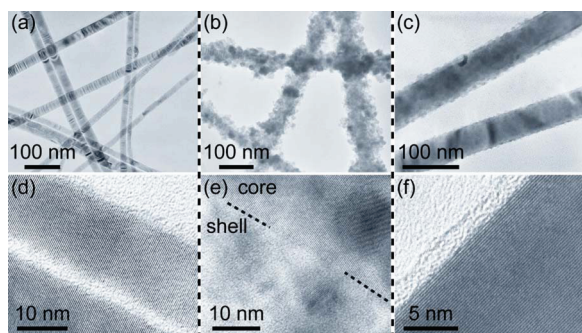
Figure 1. Representative low- and high-resolution TEM images of (a,d) CdSe, (b,e) CdSe/CdS core/shell, and (c,f) CVD grown CdSe NWs.

to synthesize a third set of CdSe NWs with an average radius of 32 ± 26 nm (unpublished). Representative low- and high-resolution transmission electron microscope (TEM) images of the NWs are shown in Figure 1a−f. More details about each synthesis can be found in the Experimental Section.

Initial results measuring ρ_{exc} at two wavelengths for all three samples are illustrated in Figure 2a−c. Specifically, single NW emission intensities are plotted as a function of excitation polarization angle relative to the NW growth axis for two wavelengths, 486 nm (2.55 eV) and 640 nm (1.94 eV). For clarity, all emission intensities have been scaled to enable midpoints of both the 486 and 640 nm traces to coincide. Corresponding emission images at selected angles have also been provided (Figure 2d−f) to illustrate how single wire emission images change with incident polarization angle.

In all samples, clear 180° oscillations in the NW emission intensity are seen. However, apparent differences between the 486 and 640 nm traces also exist in Figure 2b,c for either CdSe/CdS or CVD CdSe NWs. Namely, in both cases, the peak to valley ratio for the 486 nm trace is suppressed relative to that of the 640 nm trace. As a

consequence, the data suggest that the excitation polarization anisotropy of these NWs changes with excitation frequency. By contrast, in CdSe NWs, no significant variation between the two curves exists (Figure 2a), consistent with previous studies we have conducted on ρ_{exc} wavelength sensitivities for ~ 3 and ~ 11 nm radii CdSe NWs.[24] These studies, conducted in both air and polymethylmethacrylate (PMMA) show no wavelength sensitivities despite structure in the linear absorption of thinner wires, suggesting confinement effects. Apparent wavelength-dependent ρ_{exc}-values therefore appear to occur only for thick NWs with radii exceeding ~ 25 nm.

To better explore these apparent size- and wavelength-dependent ρ_{exc} variations, we have conducted more quantitative studies. In particular, photoluminescence images of single CdSe, CdSe/CdS, and CVD CdSe NWs were obtained under parallel and perpendicularly polarized excitation at nine wavelengths between 640 and 486 nm. Resulting experimental ρ_{exc}-values are shown in Figure 3a−c. Clear ρ_{exc} rolloffs with decreasing excitation wavelength are apparent for individual CdSe/CdS (Figure 3b) and CVD CdSe NWs (Figure 3c). This again differs from the case of bare CdSe NWs (Figure 3a), which do not exhibit such rolloffs. Furthermore, differences in the apparent magnitude of the rolloff between bare and core/shell wires likely arise from the additional attenuation of the incident optical field by the CdS shell which suppresses parallel fields inside the wire while enhancing complementary perpendicular fields. This, in turn, leads to larger decreases in ρ_{exc} values with increasing excitation frequency.

In all three cases, insets show the behavior of an individual NW to further illustrate ρ_{exc} variations at short wavelengths. For example, a prominent rolloff, outside the error bars of the main plot, can be seen in the inset
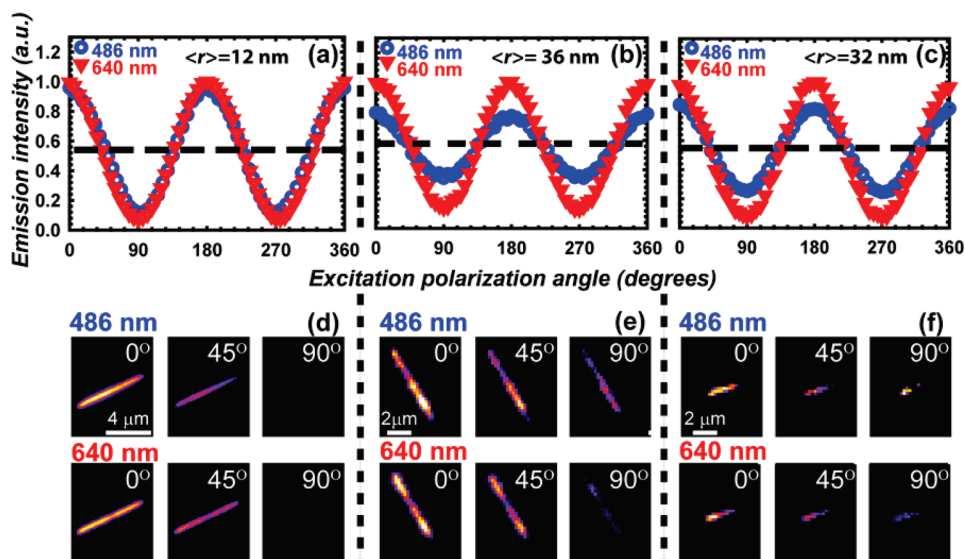

Figure 2. Single NW emission intensities plotted against excitation polarization angle along with corresponding emission images at fixed angles for (a,d) CdSe, (b,e) CdSe/CdS, and (c,f) CVD CdSe NWs at two colors, 486 and 640 nm.
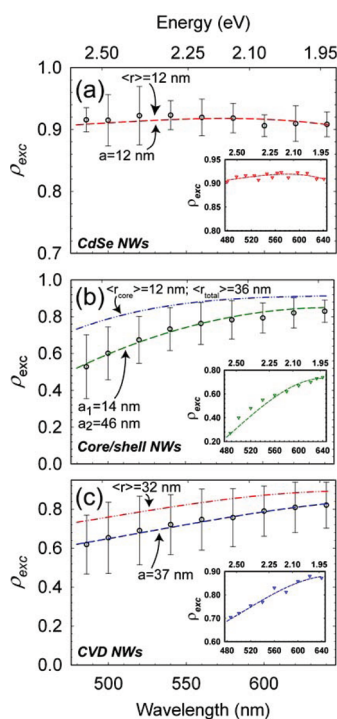
Figure 3. Average ρ_{exc}-values plotted against excitation wavelength for (a) CdSe, (b) CdSe/CdS, and (c) CVD CdSe NWs. In each case, insets illustrate data taken from a single NW. All dashed lines are theoretical fits based on a model discussed in the text using a best fit radius (dashed line) and the actual experimental average radius (dash/dot line) of the ensemble.

of Figure 3b. This illustrates significant variations in CdSe/CdS NW spectral polarization sensitivities that can be attributed to variations in wire-to-wire shell thicknesses and core radii.[33] All observations thus confirm the existence of ρ_{exc} wavelength dependencies in optically thick NWs and, more importantly, demonstrate the onset of a transition between dielectric contrast influences in nanostructures and bulk-like behavior.

Polarization Anisotropy Model for Bare and Core/Shell NWs. To quantitatively explain the observed size-dependent response, we have modeled the absorption of polarized light by NWs for two limiting cases where the incident light polarization vector is (a) parallel and (b) perpendicular to the NW growth axis. Both calculations entail solving for the electric and magnetic fields of the transmitted light inside a NW (radius a) possessing a complex frequency-dependent dielectric constant $\varepsilon(\omega)$. The wire is assumed to be oriented as shown in Supporting Information Figure S.1a, where the NW growth axis points along the z direction of a Cartesian coordinate system and light impinges upon it normal to this direction. The wire is also assumed to be embedded in a homogeneous medium with a complex dielectric constant $\varepsilon_M(\omega)$. Note that the current study is different from prior calculations of the absorption anisotropy in thick NWs,[6] where the limiting case of a nonabsorbing (or weakly absorbing) NW was considered. In the current study, the case of a strongly absorbing NW is considered through explicit used of its *complex*, frequency-dependent NW dielectric constant.

Transmitted Electric and Magnetic Fields. General expressions for the transmitted electric ($\mathbf{E}_T$) and magnetic fields ($\mathbf{H}_T$) were obtained from ref 34 which describes the extinction of a circular dielectric cylinder embedded in an absorbing medium. For the case where the incident light polarization vector is parallel to the NW growth axis (Supporting InformationFigure S1b), expressions for the transmitted electric and magnetic fields are

$$\mathbf{E}_T^{\parallel}(r, \phi) = E_{0\parallel} \sum_{n=-\infty}^{\infty} i^n c_n J_n(kr)\, e^{in\phi}\, \hat{z} \tag{1}$$

$$\mathbf{H}_T^{\parallel}(r, \phi) = \frac{E_{0\parallel}}{Zk}\sqrt{\varepsilon(\omega)} \sum_{n=-\infty}^{\infty} i^n c_n \frac{n}{r} J_n(kr)\, e^{in\phi}\, \hat{r} +$$
$$\frac{iE_{0\parallel}}{Z}\sqrt{\varepsilon(\omega)} \sum_{n=-\infty}^{\infty} i^n c_n J'_n(kr)\, e^{in\phi}\, \hat{\phi} \tag{2}$$

where $E_{0\parallel}$ is the incident electric field magnitude, Z is the wave impedance of free space ($Z = (\mu_0/\varepsilon_0)^{1/2}$), μ_o (ε_o) is the permeability (permittivity) of free space, $k = ((\varepsilon(\omega))^{1/2}2\pi)/\lambda$ is the wavenumber in the NW, n is an integer index, $\varepsilon(\omega)$ is the NW's complex frequency-dependent dielectric constant, c_n are Bessel function expansion coefficients described below, and $J_n(kr)$ are Bessel functions of the first kind with $J'_n(kr)$ their first derivatives. Note that eq 1 contains only a z component since the electric field is polarized exclusively along the NW growth axis. Likewise, the first (second) component in eq 2 is the radial (angular) contribution of the magnetic field vector.

Analogous expressions for the electric and magnetic field when the polarization vector is perpendicular to the NW growth axis (Supporting Information Figure S.1c) are

$$\mathbf{E}_T^{\perp}(r, \phi) = -\frac{E_{0\perp}}{k} \sum_{n=-\infty}^{\infty} i^n d_n \frac{n}{r} J_n(kr)\, e^{in\phi}\, \hat{r} -$$
$$iE_{0\perp} \sum_{n=-\infty}^{\infty} i^n d_n J'_n(kr)\, e^{in\phi}\, \hat{\phi} \tag{3}$$

$$\mathbf{H}_T^{\perp}(r, \phi) = \frac{E_{0\perp}}{Z}\sqrt{\varepsilon(\omega)} \sum_{n=-\infty}^{\infty} i^n d_n J_n(kr)\, e^{in\phi}\, \hat{z} \tag{4}$$

where $E_{0\perp}$ is the incident electric field magnitude and d_n is a Bessel function expansion coefficient described below. This time, the first (second) term in eq 3 is the radial (angular) contribution of the electric field vector. Furthermore, eq 4 contains only one component since the magnetic field is polarized exclusively along the NW growth axis.

Expressions for the coefficients c_n and d_n in eqs 1−4 can be obtained by imposing appropriate electromagnetic boundary conditions[35] at the NW surface. Namely,

$$\varepsilon_M(\omega)E_1^n = \varepsilon(\omega)E_2^n \qquad (5)$$

$$\mu_1 H_1^n = \mu_2 H_2^n \qquad (6)$$

$$\mathbf{E}_1^t = \mathbf{E}_2^t \qquad (7)$$

$$\mathbf{H}_1^t = \mathbf{H}_2^t \qquad (8)$$

where $\mathbf{E}_1 = \mathbf{E}_I + \mathbf{E}_S$, $\mathbf{E}_2 = \mathbf{E}_T$, $\mathbf{H}_1 = \mathbf{H}_I + \mathbf{H}_S$, $\mathbf{H}_2 = \mathbf{H}_T$, and $\mu_1 = \mu_2 = 1$ because the NWs are nonmagnetic. $\mathbf{E}_I$ and $\mathbf{E}_S$ ($\mathbf{H}_I$ and $\mathbf{H}_S$) denote the incident and scattered electric (magnetic) fields. In eqs 5 and 6, E_1^n, E_2^n, H_1^n, and H_2^n denote the magnitudes of the components of $\mathbf{E}_1$ or $\mathbf{E}_2$ and $\mathbf{H}_1$ or $\mathbf{H}_2$ normal to the NW surface. In eqs 7 and 8, though vector quantities $\mathbf{E}_1^t$, $\mathbf{E}_2^t$, $\mathbf{H}_1^t$, and $\mathbf{H}_2^t$ are specified, in practice, the magnitude of their components tangential to the NW surface (see Supporting Information Figure S.2a,b) are considered to be continuous across the boundary. By applying eq 5–8, one then finds relevant forms of the Bessel function weighting coefficients

$$c_n = \frac{\sqrt{\varepsilon_M(\omega)}H_n'(k_0 a)J_n(k_0 a) - \sqrt{\varepsilon_M(\omega)}H_n(k_0 a)J_n'(k_0 a)}{\sqrt{\varepsilon_M(\omega)}H_n'(k_0 a)J_n(ka) - \sqrt{\varepsilon(\omega)}H_n(k_0 a)J_n'(ka)}$$

$$(9)$$

$$d_n = \frac{\sqrt{\varepsilon_M(\omega)}H_n(k_0 a)J_n'(k_0 a) - \sqrt{\varepsilon_M(\omega)}J_n(k_0 a)H_n'(k_0 a)}{\sqrt{\varepsilon_M(\omega)}J_n'(ka)H_n(k_0 a) - \sqrt{\varepsilon(\omega)}J_n(ka)H_n'(k_0 a)}$$

$$(10)$$

In eqs 9 and 10, $H_n(k_0 a)$ are complementary Hankel functions of the first kind, $H'_n(k_0 a)$ are their first derivatives, and $k_0 = ((\varepsilon_M(\omega))^{1/2}2\pi)/\lambda$ is the wavenumber in the surrounding medium. More details about the derivation of eqs 1–10 can be found in the Supporting Information.

To account for the case of a core/shell NW, we derive analogous expressions for $\mathbf{E}_T$ and $\mathbf{H}_T$ in the *core* of such wires involving the use of additional boundary conditions (see Supporting Information). In this case, the complex dielectric constant of the core (shell) is denoted by $\varepsilon_2(\omega)$ [$\varepsilon_1(\omega)$]. Likewise, the core (total NW) radius is denoted by a_1 (a_2) (Supporting Information Figure S.3). Resulting expressions for $\mathbf{E}_T$ and $\mathbf{H}_T$ are identical to those in eqs 1–4 with two exceptions, the first being that the argument of all Bessel functions is ($k_2 r$) as opposed to (kr). Second, they employ different Bessel function expansion coefficients, which we denote using f_n (replacing c_n in eqs 1 and 2) and g_n (replacing d_n in eq 3 and 4). Derived expressions for f_n and g_n can be found in the Supporting Information (eqs S.83 and S.91).

NW Absorption Rates. Given the above expressions for $\mathbf{E}_T$ and $\mathbf{H}_T$, we now determine NW absorption rates for parallel and perpendicularly polarized light. This is accomplished using the complex Poynting vector field transmitted ($\mathbf{S}_T$) through the wire where $\mathrm{Re}[\mathbf{S}] = \mathrm{Re}[\mathbf{E} \times \mathbf{H}^*]$ is the time-averaged intensity of energy flow at a given
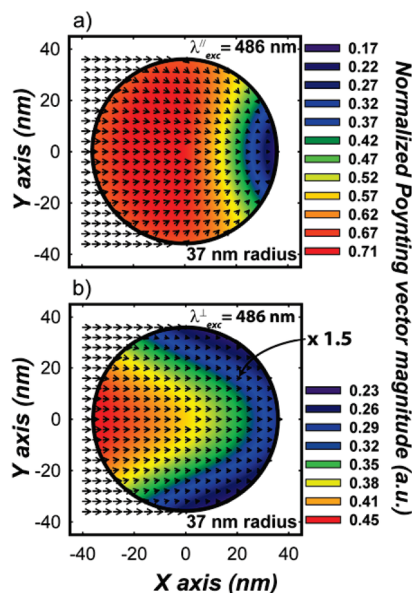

Figure 4. Calculated Poynting vector fields inside a 37 nm radius CdSe NW for (a) parallel and (b) perpendicularly polarized light excitation at 486 nm.

point within the wire, oriented along the light propagation direction.[36] Specifically, we evaluate $\mathrm{Re}[\mathbf{S}_T^{\parallel}] = \mathrm{Re}[\frac{1}{2}\mathbf{E}_T^{\parallel} \times \mathbf{H}_T^{\parallel *}]$ and $\mathrm{Re}[\mathbf{S}_T^{\perp}] = \mathrm{Re}[\frac{1}{2}\mathbf{E}_T^{\perp} \times \mathbf{H}_T^{\perp *}]$ to account for both incident light polarizations.

To illustrate, Figure 4 depicts the calculated complex Poynting vector fields, $\mathrm{Re}[\mathbf{S}_T^{\parallel}]$ and $\mathrm{Re}[\mathbf{S}_T^{\perp}]$, inside a 37 nm radius CdSe NW when illuminated at 486 nm. In the vector plot, the incident complex Poynting vector field (*i.e.*, the beam) approaches the NW from the left. For clarity, the vectors in the perpendicular excitation plot have been scaled by a factor of 1.5 to make them more apparent. In either case, the underlying (color) contour plots represent the magnitude of $\mathrm{Re}[\mathbf{S}_T^{\parallel}]$, normalized to the incident intensity, at a given point inside the wire. Additional vector plots for 640 nm excitation as well as for the case of a 12 nm radius NW can be found in the Supporting Information (Figure S.3). Subsequently by evaluating the divergence of $\mathrm{Re}[\mathbf{S}_T]$ ($\nabla \cdot \mathrm{Re}[\mathbf{S}_T]$) we obtain a quantitative picture of where the optical energy dissipates within the wire since large areas of *negative* divergence represent regions of significant absorption.[36]

Figure 5 depicts NW cross-sectional profiles illustrating energy dissipation for parallel and perpendicularly polarized light. Specifically, the divergence of $\mathrm{Re}[\mathbf{S}_T^{\parallel}]$ and $\mathrm{Re}[\mathbf{S}_T^{\perp}]$ for a 37 nm radius CdSe NW excited at 486 nm are plotted. Additional contour plots, illustrating the divergence at 640 nm, as well as for a 12 nm radius NW excited at 486 and 640 nm can be found in the Supporting Information (Figure S.4).

Next, to calculate the total power absorbed by the wire for a given unit length we integrate the divergence over a unit NW volume. For simplicity, the divergence theorem is used to construct an expression for
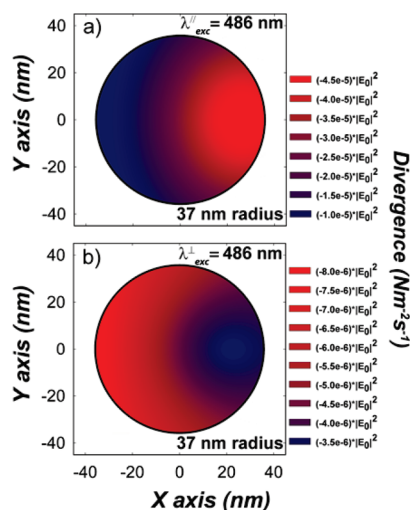
Figure 5. Calculated Poynting vector divergence inside a 37 nm radius CdSe NW for (a) parallel and (b) perpendicularly polarized light excitation at 486 nm.

the power absorbed in terms of the Poynting vector flux across the NW surface[34]

$$W = -\text{Re}[\int_0^{2\pi} \mathbf{S}_T \cdot a d\phi \hat{r}] = -\frac{1}{2}\text{Re}[\int_0^{2\pi} [\mathbf{E}_T \times \mathbf{H}_T^*] \cdot a d\phi \hat{r}]$$

(11)

The integration is carried out with $r = a$ for bare wires and with $r = a_1$ for core/shell NWs since we monitor the core absorption *via* its emission intensity in excitation experiments. When eqs 1−4, 9 and 10 (or analogous expressions for core/shell wires) are introduced into eq 11, the following parallel/perpendicular polarization energy absorption rates are obtained for bare NWs (or core/shell NWs when c_n and d_n are replaced with f_n and g_n, respectively, and a is replaced with a_1)

$$W^{\parallel} = \frac{\pi a}{Z}|E_{0\parallel}|^2 \text{Re}\{-i \sum_{n=-\infty}^{\infty} \sqrt{\varepsilon(\omega)}^* |c_n|^2 J_n(ka) J_n'^*(ka)\}$$

(12)

$$W^{\perp} = \frac{\pi a}{Z}|E_{0\perp}|^2 \text{Re}\{i \sum_{n=-\infty}^{\infty} \sqrt{\varepsilon(\omega)}^* |d_n|^2 J_n'(ka) J_n^*(ka)\}$$

(13)

More information about these calculations can be found in the Supporting Information.

Theoretical excitation polarization anisotropies are then evaluated using $\rho_{\text{exc}} = (W^{\parallel} - W^{\perp})/(W^{\parallel} + W^{\perp})$. Model results are illustrated as dashed and dashed/dotted lines in Figure 3a−c. In the absence of actual NW $\varepsilon(\omega)$-values, bulk frequency-dependent dielectric constants of CdSe and CdS were used.[37] Furthermore, a value of $\varepsilon_M = 1.0$ (air) was employed for the surrounding medium's dielectric constant though all prior expressions are general to complex ε_M values. Best fits to the data (dashed lines) by eye were obtained assuming the following values for the NW radii a, a_1, and a_2 [$a = 12$ nm (CdSe), $a_1 = 14$ nm ($a_2 = 46$ nm) (CdSe/CdS), and

$a = 37$ nm (CVD CdSe)]. Additional fits using experimentally measured average radii from each ensemble [$a \approx 12$ nm (CdSe), $a_1 \approx 14$ nm ($a_2 \approx 36$ nm) (CdSe/CdS), $a \approx 32$ nm (CVD CdSe)] are also shown as dash/dotted lines. In either case, the model and experiment agree well with each other and, more importantly, confirm observed ρ_{exc} rolloffs at short wavelengths in core/shell CdSe/CdS and CVD grown CdSe NWs.

Absorption Cross-Sections. Finally, expressions for the NW linear absorption cross-section (σ) were obtained using the above results. These values are important physical parameters that enable one to quantify NW concentrations, emission quantum yields as well as the number of photogenerated carriers in optical experiments. However, despite their usefulness, such numbers are not common and to the best of our knowledge only two studies exist on the subject for NWs. Specifically, NW cross-sections have previously been measured experimentally for CdSe and CdTe NWs at wavelengths across the visible.[38] In tandem, a back of the envelope expression was used to estimate CdSe NW cross-sections at wavelengths far to the blue of the band edge in ref 39.

The present approach involving $\mathbf{E}_T$ and $\mathbf{H}_T$ allows us to rigorously calculate the total power absorbed by a NW of unit length at all frequencies. In turn, we obtain formal expressions for the NW absorption cross-section applicable, not just to CdSe NWs, but to other 1D systems as well when embedded in a nonabsorbing medium. The only requirement involves having appropriate values of the NW's frequency-dependent dielectric constant (or refractive index). In the current example, we use tabulated bulk $\varepsilon(\omega)$ values in the absence of actual NW numbers.

In general, the amount of power absorbed by a unit NW length in a *nonabsorbing* medium is $P_{\text{abs}} = W = \sigma I$, where I is incident light intensity and is given by the magnitude of its complex Poynting vector, $I = |\text{Re}[\mathbf{S}_I]| = (\varepsilon v |\mathbf{E}_I|^2)/2$ (assuming plane wave excitation in a dielectric characterized by ε and by v, the speed of the wave in it). Note that a nonabsorbing medium is specified even though all prior expressions (eq 1−15) are general to an absorbing medium. The distinction occurs here because the above expression for I is only valid for a nonabsorbing medium. Furthermore, it readily yields analytical solutions. The general case of an absorbing medium is more complicated and must be solved numerically. The reader may thus refer to ref 34 for more details. With this said, both $\sigma^{\parallel}$ and $\sigma^{\perp}$ are derived using eqs 12 and 13, yielding

$$\sigma^{\parallel}(\omega) = \frac{2\pi a}{Z\varepsilon v}\text{Re}\{-i \sum_{n=-\infty}^{\infty} \sqrt{\varepsilon(\omega)}^* |c_n|^2 J_n(ka) J_n'^*(ka)\}$$

(14)

and

$$\sigma^{\perp}(\omega) = \frac{2\pi a}{Z\varepsilon v} \mathrm{Re}\{i \sum_{n=-\infty}^{\infty} \sqrt{\varepsilon(\omega)}^* |d_n|^2 J'_n(ka) \, J^*_n(ka)\}$$

(15)

To account for randomly oriented NWs, these absorption cross-sections are then angle averaged

$$\langle \sigma \rangle = \frac{1}{2} \int_0^\pi (\sigma^{\parallel} \cos^2(\theta) + \sigma^{\perp} \sin^2(\theta)) \sin(\theta) \, d\theta$$

(16)

giving average NW cross-sections where θ is the angle between the NW growth axis and the light's polarization vector. Subsequent evaluation of eq 16 leads to $\langle \sigma \rangle = (\sigma^{\parallel} + 2\sigma^{\perp})/3$.

Calculated $\sigma^{\parallel}$, $\sigma^{\perp}$, and $\langle \sigma \rangle$ values are presented in Figure 6 for an 11 nm radius CdSe NW in air. Notably, these values are in good agreement with reported experimental numbers. To illustrate, the predicted $\sigma^{\parallel}$ ($\sigma^{\perp}$) value at 488 nm is $\sigma^{\parallel} \approx 1.81 \times 10^{-10}$ cm^2/μm ($\sigma^{\perp} \approx 8.49 \times 10^{-12}$ cm^2/μm) while the experimental value for the same radius NW is $\sigma^{\parallel} \approx 1.45 \times 10^{-10}$ cm^2/μm ($\sigma^{\perp} \approx 6.85 \times 10^{-12}$ cm^2/μm).[38] Corresponding average values are: model $\langle \sigma \rangle = 6.61 \times 10^{-11}$ cm^2/μm; experiment $\langle \sigma \rangle = 5.30 \times 10^{-11}$ cm^2/μm.

Given that eqs 14−16 are general expressions applicable to any NW embedded in a nonabsorbing medium through the appropriate choice of $\varepsilon(\omega)$, NW cross-sections for both thick and thin wires can be determined in the absence of actual experimental val-
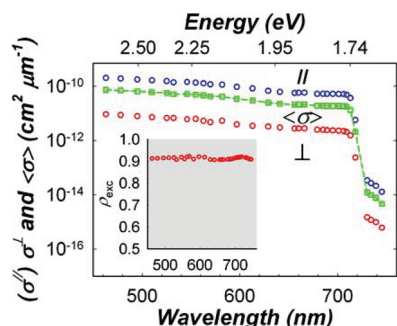

Figure 6. Parallel ($\sigma^{\parallel}$), perpendicular ($\sigma^{\perp}$) and angle averaged ($\langle \sigma \rangle$) linear absorption cross-sections determined for a 11 nm radius CdSe NW using theoretical expressions described in the text. The dashed line is simply a guide to the eye. Insets shows predicted ρ_{exc}-values.

ues. This illustrates the general usefulness of the model. More details about these expressions and a sample absorption cross-section calculation can be found in the Supporting Information.

CONCLUSIONS

The present study focuses on better understanding the excitation polarization anisotropy of optically thick NWs where dielectric contrast influences compete with the onset of bulk-like properties. Obtained results complement prior measurements we and others have conducted to elucidate dielectric contrast *versus* confinement-induced contributions to the polarization anisotropy of (narrow diameter) NWs. More importantly, while these earlier studies suggest dominant dielectric contrast influences in NWs, data from the current study show a prominent wavelength-dependent NW excitation polarization anisotropy in thick ($r > ca.$ 25 nm) wires prepared using a variety of methods including solution- and CVD-based chemistries. The current study therefore represents the first quantitative experimental investigation into the radial dependencies of NW excitation polarization anisotropies in the limiting size regime where dielectric contrast effects begin to compete with the onset of bulk like behavior.

Experimental ρ_{exc}-values have subsequently been modeled by treating the NW as an absorbing dielectric cylinder under plane wave excitation. Theoretical anisotropies have then been obtained by solving for the Poynting vector field and its associated divergence inside a NW where comparisons to experimental anisotropies yield good agreement and, in particular, successfully reproduce the above decrease in NW ρ_{exc}-values with increasing NW radius at blue wavelengths. In tandem, the derived model produces rigorous, yet general, expressions for the NW absorption cross-section in a nonabsorbing medium with predicted values in excellent agreement with prior experimental results. Thus the derived model enables one to make estimates of both ρ_{exc}-values as well as NW absorption cross-sections in the absence of actual experimental values, which should prove useful in better characterizing the optical response of this and other 1D systems.

EXPERIMENTAL SECTION

CdSe and Core/Shell CdSe/CdS NW Syntheses. CdSe NWs were synthesized following a SLS growth scheme documented in refs 28−31. Briefly, low-melting bimetallic Au/Bi core/shell nanoparticles (~2 nm diameter)[32] were used to catalyze the nucleation and growth of NWs in a reaction mixture consisting of trioctylphosphine oxide (TOPO), trioctylphosphine selenide (TOPSe), cadmium oxide, and octanoic acid. Workup of the resulting product was conducted as described in ref 31.

A portion of the resulting core NWs was then overcoated with CdS using a procedure described in ref 33. In particular, NWs were first "washed" multiple times with toluene and pyridine to remove as much surface bound surfactant as possible.

Wires were then resuspended in squalane followed by the slow introduction of dimethylcadmium (CdMe$_2$) and bis(trimethylsilyl)sulfide [(TMS)$_2$S] at 250 °C. Resulting core/shell wires were then processed as described in ref 33.

CdSe NW CVD Synthesis. Approximately 50 μL of a 0.38 mM (19 nmoles) Au/Bi NP solution was dropcast onto a silicon substrate which was eventually placed at the center of a tube furnace. Cadmium and selenium precursors were then introduced into the reaction chamber by bubbling nitrogen through two separate solutions of CdMe$_2$ and (TMS)$_2$Se in hexane. Typical metal and chalcogen stock solution concentrations were 0.05 and 0.017 M, respectively. A nitrogen flow rate of 200 cc/min was used and the reaction temperature varied between 250−400 °C. Upon

completion, silicon substrates were sonicated in toluene to recover produced NWs. The resulting suspension could then be used to prepare optical samples.

Structural Studies. All NW preparations yielded high quality wires with lengths exceeding one micrometer. Predominantly straight NW morphologies were obtained as opposed to branched structures with characteristic tripod, v-shape, and y-shape morphologies.[31] Representative low and high resolution transmission electron microscope (TEM) images are shown in Figure 1a−f with reported sizing statistics based on examining 50−100 wires per ensemble. Samples for low- and high-resolution TEM analyses were prepared by dropping a dilute solution of CdSe NWs in toluene onto ultrathin carbon-coated copper grids (Ladd). Low- and high-resolution TEM micrographs were taken with a JEOL-2010 electron microscope.

Optical Studies. Samples for optical measurements were prepared by drop-casting dilute NW suspensions onto (flamed) glass microscope coverslips. Substrates were then rinsed two or three times with toluene in order to remove any excess surfactant on the wires. All optical experiments were carried out at room temperature with at least 5 NWs studied from each ensemble. Atomic force microscopy (AFM) measurements were used to verify that steps taken to prepare optical samples yielded substantial single NW coverages. To further ensure that we examined only single wires, NWs were selected for ρ_{exc} measurements if they were not within ~5 μm of another wire and only if their emission intensity appeared relatively uniform along the wire's length.

Emission measurements were conducted using a home-built single molecule imaging instrument based around an inverted optical microscope (Nikon Eclipse TE2000-U). A grating dispersed, tunable supercontinuum white light source (Fianium) provided excitation wavelengths between 470−1700 nm (2.64−0.73 eV). Both CdSe and core/shell CdSe/CdS NWs were widefield illuminated by inserting a 400 mm focal length achromat prior to the back aperture of a high numerical aperture oil-immersion objective (Nikon 60×/1.40). The resulting excitation diameter was ~30 μm, yielding typical excitation intensities between ~2 and 11 W/cm². Because of their substantially weaker emission quantum yields, CVD-grown NWs were illuminated confocally with a ~7 μm diameter excitation spot, yielding corresponding excitation intensities between 44−194 W/cm².

NW emission was collected using the same microscope objective and was passed through a 680 nm long pass filter (Chroma) prior to being imaged on a CCD (DVC). Excitation polarization anisotropies were acquired by recording emission images from the NW subjected to linearly polarized light parallel and perpendicular to the wire's growth axis. Obtained images were then corrected for polarization orientation variations of the incident laser power.

Supporting Information Available: Derivations of **E**, **H**, and **S** for a bare NW; derivation of the power absorbed by a bare NW; derivation of the Poynting vector field divergence; derivations of **E** and **H** for a core/shell NW; sample absorption cross-section calculation. This material is available free of charge *via* the Internet at http://pubs.acs.org.

REFERENCES AND NOTES

1. Wang, J.; Gudiksen, M. S.; Duan, X.; Cui, Y.; Lieber, C. M. Highly Polarized Photoluminescence and Photodetection from Single Indium Phosphide Nanowires. *Science* **2001**, *293*, 1455–1457.
2. Sercel, P. C.; Vahala, K. J. Analytical Technique for Determining the Polarization Dependence of Optical Matrix Elements in Quantum Wires with Band-Coupling Effects. *Appl. Phys. Lett.* **1990**, *57*, 545–547.
3. Sercel, P. C.; Vahala, K. J. Polarization Dependence of Optical Absorption and Emission in Quantum Wires. *Phys. Rev. B* **1991**, *44*, 5681–5691.
4. Landau, L. D.; Lifshitz, E. M.; Pitaevskii, L. P. In *Electrodynamics of Continuous Media*; Pergamon: Oxford, U.K., 1984; pp 34−42.
5. Ruda, H. E.; Shik, A. Polarization-Sensitive Optical Phenomena in Semiconducting and Metallic Nanowires. *Phys. Rev. B* **2005**, *72*, 115308-1–115308-10.
6. Ruda, H. E.; Shik, A. Polarization-Sensitive Optical Phenomena in Thick Semiconducting Nanowires. *J. Appl. Phys.* **2006**, *100*, 024314-1-024314-6.
7. Shan, C. X.; Liu, Z.; Hark, S. K. Photoluminescence Polarization in Individual CdSe Nanowires. *Phys. Rev. B* **2006**, *74*, 153402-1–153402-4.
8. Mishra, A.; Titova, L. V.; Hoang, T. B.; Jackson, H. E.; Smith, L. M.; Yarrison-Rice, J. M.; Kim, Y.; Joyce, H. J.; Gau, Q.; Tran, H. H.; Jagadish, C. Polarization and Temperature Dependence of Photoluminescence from Zincblende and Wurtzite InP Nanowires. *Appl. Phys. Lett.* **2007**, *91*, 263104-1–263104-3.
9. Titova, L. V.; Hoang, T. B.; Jackson, H. E.; Smith, L. M.; Yarrison-Rice, J. M.; Kim, Y.; Joyce, H. J.; Tan, H. H.; Jagadish, C. Temperature Dependence of Photoluminescence from Single Core-Shell GaAs-AlGaAs Nanowires. *Appl. Phys. Lett.* **2006**, *89*, 173126-1–173126-3.
10. Qi, J.; Belcher, A. M.; White, J. M. Spectroscopy of Individual Silicon Nanowires. *Appl. Phys. Lett.* **2003**, *82*, 2616–2618.
11. Ils, P.; Greus, C.; Forchel, A.; Kulakovskii, V. D.; Gippius, N. A.; Tikhodeev, S. G. Linear Polarization of Photoluminescence Emission and Absorption in Quantum-Well Wire Structures: Experiment and Theory. *Phys. Rev. B* **1995**, *51*, 4272–4277.
12. Vouilloz, F.; Oberli, D. Y.; Dupertuis, M. A.; Gustafsson, A.; Reinhardt, F.; Kapon, E. Effect of Lateral Confinement on Valence-Band Mixing and Polarization Anisotropy in Quantum Wires. *Phys. Rev. B* **1998**, *57*, 12378–12387.
13. Akiyama, H.; Someya, T.; Sakaki, H. Optical Anisotropy in 5-nm T-Shaped Quantum Wires Fabricated by the Cleaved-Edge Overgrowth Method. *Phys. Rev. B* **1996**, *53*, R4229−R4232.
14. Tsuchiya, M.; Gaines, J. M.; Yan, R. H.; Simes, R. J.; Holtz, P. O.; Coldren, L. A.; Petroff, P. M. Optical Anisotropy in a Quantum-Well-Wire Array with Two-Dimensional Quantum Confinement. *Phys. Rev. Lett.* **1989**, *62*, 466–469.
15. Maslov, A. V.; Ning, C. Z. Radius-Dependent Polarization Anisotropy in Semiconductor Nanowires. *Phys. Rev. B* **2005**, *72*, 161310-1–161310-4.
16. Persson, M. P.; Xu, H. Q. Giant Polarization Anisotropy in Optical Transitions of Free-Standing InP Nanowires. *Phys. Rev. B* **2004**, *70*, 161310-1–161310-4.
17. Califano, M.; Zunger, A. Anisotropy of Interband Transitions in InAs Quantum Wires: An Atomic Theory. *Phys. Rev. B* **2004**, *70*, 165317-1–165317-11.
18. Zhang, X. W.; Xia, J. B. Optical Properties of GaN Wurtzite Quantum Wires. *J. Phys.: Condens. Mater.* **2006**, *18*, 3107–3115.
19. Muljarov, E. A.; Zhukov, E. A.; Dneprovskii, V. S.; Masumoto, Y. Dielectrically Enhanced Excitons in Semiconductor-Insulator Quantum Wires: Theory and Experiment. *Phys. Rev. B* **2000**, *62*, 7420–7432.
20. Han, S.; Jin, W.; Zhang, D.; Tang, T.; Li, C.; Liu, X.; Liu, Z.; Lei, B.; Zhou, C. Photoconduction Studies on GaN Nanowire Transistors Under UV and Polarized UV Illumination. *Chem. Phys. Lett.* **2004**, *389*, 176–180.
21. Yu, Y.; Protasenko, V.; Xing, H.; Jena, D.; Kuno, M. Photocurrent Polarization Anisotropy of Randomly Oriented Nanowire Networks. *Nano Lett.* **2008**, *8*, 1352–1357.

22. Singh, A.; Li, X.; Protasenko, V.; Galantai, G.; Kuno, M.; Xing, H.; Jena, D. Polarization-Sensitive Nanowire Photodetectors Based on Solution-Synthesized CdSe Quantum-Wire Solids. *Nano Lett.* **2007**, *7*, 2999–3006.

23. Kuno, M. An Overview of Solution-Based Semiconductor Nanowires: Synthesis and Optical Studies. *Phys. Chem. Chem. Phys.* **2008**, *10*, 620–639.

24. Lan, A.; Giblin, J.; Protasenko, V.; Kuno, M. Excitation and Photoluminescence Polarization Anisotropy of Single CdSe Nanowires. *Appl. Phys. Lett.* **2008**, *92*, 183110-1–183110-3.

25. Chen, H. Y.; Yang, Y. C.; Lin, H. W.; Chang, S. C.; Gwo, S. Polarized Photoluminescence from Single GaN Nanorods: Effects of Optical Confinement. *Opt. Express* **2008**, *16*, 13465–13475.

26. Fan, Z; Chang, P; Lu, J. G.; Walter, E. C.; Penner, R. M.; Lin, C; Lee, H. P. Photoluminescence and Polarized Photodetection of Single ZnO Nanowires. *Appl. Phys. Lett.* **2004**, *85*, 6128–6130.

27. Wang, F.; Dong, A.; Sun, J.; Tang, R.; Yu, H.; Buhro, W. E. Solution−Liquid−Solid Growth of Semiconductor Nanowires. *Inorg. Chem.* **2006**, *45*, 7511–7521.

28. Yu, H.; Li, J.; Loomis, R. A.; Wang, L. W.; Buhro, W. E. Two-*versus* Three-Dimensional Quantum Confinement in Indium Phosphide Wires and Dots. *Nat. Mater.* **2003**, *2*, 517–520.

29. Yu, H.; Loomis, R. A.; Gibbons, P. C.; Wang, L. W.; Buhro, W. E. Cadmium Selenide Quantum Wires and the Transition from 3D to 2D Confinement. *J. Am. Chem. Soc.* **2003**, *125*, 16168–16169.

30. Yu, H.; Buhro, W. E. Solution−Liquid−Solid Growth of Soluble GaAs Nanowires. *Adv. Mater.* **2003**, *15*, 416–419.

31. Grebinski, J. W.; Hull, K. L.; Zhang, J.; Kosel, T. H.; Kuno, M. Solution-Based Straight and Branched CdSe Nanowires. *Chem. Mater.* **2004**, *16*, 5260–5272.

32. Grebinski, J. W.; Richter, K. L.; Zhang, J.; Kosel, T. H.; Kuno, M. Synthesis and Characterization of Au/Bi Core/Shell Nanocrystals: A Precursor Toward II−VI Nanowires. *J. Phys. Chem. B* **2004**, *108*, 9745–9751.

33. Goebl, J.; Black, R.; Puthussery, J.; Giblin, J.; Kosel, T. H.; Kuno, M. Solution-Based II−VI Core/Shell Nanowire Heterostructures. *J. Am. Chem. Soc.* **2008**, *130*, 14822–14833.

34. Ruppin, R. Extinction by a Circular Cylinder in an Absorbing Medium. *Opt. Commun.* **2002**, *211*, 335–340.

35. Griffiths, D. J. In *Introduction to Electrodynamics*; Prentice Hall: NJ, 1999; pp 384.

36. Stratton, J. A. In *Electromagnetic Theory*; McGraw-Hill: New York, 1941; pp 131−137.

37. Palik, E. D. In *Handbook of Optical Constants of Solids II*; Academic Press: San Diego, CA, 1998; pp 559−578.

38. Protasenko, V.; Bacinello, D.; Kuno, M. Experimental Determination of the Absorption Cross-Section and Molar Extinction Coefficient of CdSe and CdTe Nanowires. *J. Phys. Chem. B* **2006**, *110*, 25322–25331.

39. Protasenko, V.; Hull, K. L.; Kuno, M. Disorder-Induced Optical Heterogeneity in Single CdSe Nanowires. *Adv. Mater.* **2005**, *17*, 2942–2949.